Biomolecular condensates and biogeomorphological systems exhibit a phase-separation behavior unified by a mass-conserving model

Cheng Li[1], Man-Ting Guo[2], Xiaoqing He[3, *], Quan-Xing Liu[2, *], and Zhi Qi[1, *]

[1]Center for Quantitative Biology, Peking-Tsinghua Center for Life Sciences, Academy for Advanced Interdisciplinary Studies, Peking University, Beijing 100871, China

[2]School of Mathematical Sciences, Shanghai Jiao Tong University, Shanghai 200240, China

[3]School of Mathematical Sciences, Ministry of Education Key Laboratory of Mathematics and Engineering Applications & Shanghai Key Laboratory of PMMP, East China Normal University, Shanghai 200241, China

*To whom correspondence should be addressed: zhiqi7@pku.edu.cn; qx.liu@sjtu.edu.cn; xqhe@cpde.ecnu.edu.cn

Key word: Mass-conserving reaction-diffusion system; Pattern formation; Phase separation; Biomolecular condensates; dsDNA-protein interactive co-condensates (DPICs)

Abstract

Recent research in biogeomorphology has shown that many macroscale systems exhibit spatiotemporal self-organized patterns with coarsening behaviors and also phase separation behaviors, successfully described by a mass-conserving dynamical model. Also recently, macromolecules, such as nucleic acids and proteins, have been found to assemble mesoscale biomolecular condensates inside living cells. Despite their significance, the fundamental biophysical properties of these biomolecular condensates remain poorly understood. Here, we selected DNA and the human transcription factor p53 as a model system to form a specific type of biomolecular condensate—DNA-protein interactive co-condensates (DPICs). We developed a mass-conserving dynamical model, with all parameters derived from direct experimental measurements. This model successfully reproduces the spatiotemporal dynamics of DPICs. Our findings reveal that both mesoscale biomolecular condensates and macroscale biogeomorphological systems exhibit cross-scale spatiotemporal self-organized patterns with coarsening behaviors, and cross-scale phase separation behavior. Both systems also exhibit emergent properties. Our theoretical framework offers a deeper understanding of the mechanisms underlying these phase-separation systems.

Introduction

Alan Turing first developed reaction-diffusion systems to study spatiotemporal self-organized patterns (*1*). In his seminal work, the Turing principle predicts stationary patterns with fixed characteristic length scales, arising from the symmetry-breaking of homogeneous steady states, which are described by equations such as the Swift–Hohenberg equation (*2-4*) and activator-inhibitor systems (*5, 6*). However, recent research in the field of biogeomorphology has revealed that many macroscale systems exhibit spatiotemporal self-organized patterns with coarsening behaviors. Notable examples include worm blobs, tidal flat mussel beds, and patterned ground (*7-10*). Interestingly, these macroscale biogeomorphological systems (ranging from meters to kilometers) display phase-separation behavior, an inherently demixing process analogous to the well-known oil-water phase separation phenomenon.

To describe the coarsening processes and equilibrium phases during pattern formation, the Flory–Huggins and Cahn–Hilliard approaches have been widely employed to minimize the total free energy of the system (*9, 11-16*). In binary mixtures, these theories have provided valuable thermodynamic equilibrium frameworks for investigating phase separation (*17-20*). However, understanding the nucleation and growth processes, especially in systems with numerous local minima and energy barriers, remains a significant challenge. Additionally, connecting parameters related to entropy and enthalpy with real biophysical parameters measured from experiments is particularly difficult. These shortcomings can be addressed by a mechanism-based modeling approach, specifically through the use of mass-conserving dynamical models. Compared to the Turing principle, scientists have found that the mass-conserving dynamical models are more effective for studying the detailed processes and mechanisms of spatiotemporal self-organized patterns with coarsening behaviors (*8-10*).

Macromolecules inside living cells, such as nucleic acids and proteins, have been identified to assemble mesoscale biomolecular condensates (*21, 22*), which play critical roles in cellular organization and physiology (*23*). These biomolecular condensates also exhibit dynamical patterns with coarsening behaviors. Despite the considerable attention given to biomolecular condensates in recent years, there are still many questions unanswered. For instance, whether we can develop a mass-conserving dynamical model—akin to those successfully employed in describing the aggregation of organisms and pebbles in biogeomorphological systems—to reproduce the spatiotemporal dynamics of mass-conserved biomolecular condensates? Can we also demonstrate these biomolecular condensates exhibit phase separation behavior and emergent properties?

To elucidate the underlying mechanistic principles, we focused on a particular type of biomolecular condensate: a truncated version of the human transcription factor p53, which, in conjunction with double-stranded DNA (dsDNA), can give rise to dsDNA-protein interactive co-condensates (DPICs) (Fig. 1A) (*24*). Notably, neither dsDNA nor the protein undergoes phase separation independently. The system remains closed and mass-conserved throughout the formation of DPICs.

Previous studies have demonstrated that the aggregation of organisms and pebbles in biogeomorphological systems can be effectively described by a set of response functions encompassing both positive and negative local concentration-dependent feedback mechanisms (*8-10, 25*). These findings strongly suggest that only systems exhibiting such features can be effectively modeled using mass-conserving dynamical approaches. To explore this concept in the context of DPICs, we designed a series of experiments to test the response functions governing the exchange between the outside and inside the DPIC, as well as to measure the microscopic behavioral parameters within the system. These parameters were then incorporated into a mass-conserving dynamical model to simulate the formation process of DPICs. Numerical simulations of our model successfully reproduced phase diagrams and spatiotemporal scale-invariance of the DPIC formation. Dispersion relation analyses of both our experiment and the model reveal that DPICs exhibit a phase separation feature. Further analysis demonstrates that these DPICs also exhibit emergent properties. These findings provide valuable insights into the dynamic mechanisms underlying the formation of DPIC patterns, and underscore that despite significant differences in spatiotemporal scales of the patterns, biomolecular condensates (ranging from nanometers to micrometers and from seconds to minutes) and biogeomorphological systems (ranging from meters to kilometers and from days to years) exhibit similar pattern formation and coarsening behaviors.

Results

DPICs exhibit both positive and negative local concentration-dependent dynamic behaviors of proteins

Our previous investigations have demonstrated that a truncated version of the human transcription factor p53, referred to as $p53^{4M}$ ΔTAD, in conjunction with dsDNA, can give rise to DPICs (Fig. 1A) (*24*). This mutant lacks the amino-terminal transactivation domain (TAD, 1-62) and contains mutations in four residues (M133L/V203A/N239Y/N268D) within the DNA-binding domain (DBD) (Supplementary Fig. 1A & **Methods**). Following the protocol outlined in previous study (*24*), we purified the p53 variant "$p53^{4M}$ ΔTAD" *in vitro* (Supplementary Fig. 1B) and conducted electrophoretic mobility shift assays

(EMSAs) to confirm the DNA-binding affinity and sequence selectivity (Supplementary Fig. 1C), validating its activity.

Upon mixing 20 μM $p53^{4M}$ ΔTAD labeled with ATTO565 and 0.6 μM 400-bp random dsDNA labeled with FAM for 0.5 hours, droplet-like DPICs formed (Fig. 1A). To scrutinize the intricate details of DPICs, we conducted *in vitro* droplet assays, systematically combining concentrations of 0, 0.15, 0.3, 0.6, and 0.9 μM 400-bp random DNA labeled with DAPI with 0, 2.5, 5, 10, 20, and 40 μM dark $p53^{4M}$ ΔTAD, thereby constructing a phase diagram (Supplementary Fig. 1D) (*24*). It is pertinent to mention that the working buffer employed in our experiments maintained the physiological conditions (8 mM Tris-HCl (pH 7.5) and 120 mM NaCl) and contained no crowding agents. Furthermore, all referenced p53 concentrations pertain to the monomeric form.

We then investigated whether the DPIC system exhibits local concentration-dependent feedback mechanisms, which are crucial for establishing the mass-conserving dynamical model. Throughout the formation process of DPICs, the total amount of free protein and DNA-bound protein remains conserved. This conservation also applies to the dsDNA. Previous fluorescence recovery after photobleaching (FRAP) experiments have demonstrated that the motility of long dsDNA is significantly lower than that of proteins inside the DPIC (Supplementary Fig. 2A), and other methods demonstrated that the DPIC formation comes from the capacity of p53 to bridge different DNA duplexes (*24*). Additionally, fluorescence correlation spectroscopy (FCS) has shown that the diffusion coefficient of dsDNA is lower than that of proteins outside the DPIC (Supplementary Fig. 2B). Thus, DNA primarily functions as a scaffold that promotes the conversion of free proteins into DNA-bound proteins. The role of DNA is treated as a parameter in our dynamic model of DPICs. Regions enriched with DNA-bound proteins represent the DPICs, while areas with low densities of DNA-bound proteins are considered outside the DPICs.

Here, we emphasize that the fundamental principles of activator–inhibitor or activator–depletion models are well-established for generating Turing patterns (*5, 26*). However, the dynamics of our DPICs are distinct in that they do not rely on the production and dissipation of proteins but rather on the conversion between free proteins and DNA-bound proteins. Therefore, we propose using a mass-conserving reaction–diffusion model to study DPICs. Consequently, our model involves two variables describing the concentrations of DNA-bound protein (u) and free protein (v) (Session 1.1 in **Supplementary Methods**). It is pertinent to note that in the subsequent sections, mathematical symbols with a tilde denote the fluorescent intensity measured from experiments, whereas symbols without a tilde represent concentration.

To directly assess the presence of local concentration-dependent positive feedback within DPICs, which is the first response function, we devised an *in vitro* droplet assay, termed the "recruitment experiment" (Fig. 1B(i)). Initially, we mixed 20 μM unlabeled p53^{4M} ΔTAD with 0.6 μM FAM-labeled 400-bp random dsDNA for a 20-minute incubation to generate DPICs. Subsequently, we removed all unbound protein and DNA. Finally, we introduced 20 μM ATTO565-labeled p53^{4M} ΔTAD and observed a rapid infiltration of red-fluorescent proteins into the original green DPICs (Fig. 1B(ii)). The time traces of ATTO565-labeled p53^{4M} ΔTAD intensities were quantified, revealing that protein recruitment reached equilibrium after approximately one hour (N = 41, Supplementary Fig. 3). We found a significant positive correlation (Fig. 1B(iii)) between the intensity of recruited ATTO565-labeled p53^{4M} ΔTAD at equilibrium (3,540 s in Supplementary Fig. 3B(ii)) and the initial amount of p53^{4M} ΔTAD inside the DPIC (0 s, Supplementary Fig. 4B(v) and **Methods**). This indicates a positive feedback mechanism between protein recruitment and local concentration of protein. A recruitment function, $\tilde{f}(\tilde{u}) = k_1\tilde{u} + \tilde{b}$, was used to fit the experimental data well: (i) $k_1 = 1.35 \pm 0.05$, the recruitment rate coefficient (Supplementary Table 1); (ii) $\tilde{b} = 93 \pm 56$, the self-triggered rate (Supplementary Table 1).

To quantify the presence of local concentration-dependent negative feedback within DPICs, we devised a series of *in vitro* droplet assays termed "escape experiments" (Fig. 1C(i) & Supplementary Fig. 5A). Initially, we incubated ATTO565-labeled p53^{4M} ΔTAD and FAM-labeled 400-bp random dsDNA for 45 minutes at room temperature to generate large dual-color DPICs. After removing all unbound protein and DNA, we introduced a blank working buffer and began recording the time traces of ATTO565-labeled p53^{4M} ΔTAD intensities. We prepared a total of 15 different experimental conditions of DPICs by varying the initial protein and DNA concentrations (Supplementary Fig. 5A-B), selecting the condition with 10 μM ATTO565-labeled p53^{4M} ΔTAD and 0.3 μM FAM-labeled 400-bp random dsDNA as a representative example (Fig. 1C(ii)). We observed a gradual decrease in protein intensity under this condition, consistent with all other experimental setups (Supplementary Fig. 5C). To mitigate potential photobleaching effects, we collected data at only six time points from 0 to 18 hours post-injection. The declining protein intensity suggested that protein molecules were indeed escaping from the DPICs. This escaping behavior stabilized after 18 hours (Supplementary Fig. 5D), with the escape ratio of proteins at the 18-hour time point showing a pronounced negative correlation with the normalized initial amount of p53^{4M} ΔTAD inside DPIC at 0-hour time point (Fig. 1C(iii)). This indicates a negative feedback mechanism between the ratio of protein escaped from the DPIC and the local concentration of protein inside the DPIC. An escape function, $\tilde{g}\,(\tilde{u}, \tilde{v}) = \frac{\beta}{\beta+\tilde{u}+\tilde{v}}$, was used to fit these experimental data well: $\tilde{v} = 0.5$ (A small value from the experimental estimation), $\beta = 1.6 \pm 0.4$, the half-saturation constant (Supplementary Table 1).

Taken together, our p53-DNA DPIC system encompasses two types of response functions: the first describes the participation of free proteins in the formation of DPICs, and the second delineates the transformation of DPIC-bound proteins back into free proteins.

A mass-conserving dynamical model for DPICs

Mass-conserving dynamical models have proven effective in elucidating spatiotemporal self-organized patterns with coarsening behaviors across various systems, including animal and pebble aggregations (*8-10*) as well as cell polarity aggregation (*25, 27, 28*). To explore whether a similar mass-conserving model could be applied to understand the formation behaviors of DPICs, we utilized the two response functions discussed earlier (Fig. 2A(i)).

For any given spatial point (x, y) at time t, the change of DNA-bound protein, $u(x, y, t)$, depend on concentration of components within radius Δx (Fig. 2A(ii)), and the profiles of $u(x, y, t)$ reflects where the proteins are clustered to form DPICs.

The dynamics of u and v are governed by the equation (1) (Fig. 2A(iii)):

$$\begin{cases} \frac{\partial u}{\partial t} = \underbrace{-k_d u + f(u)v - \rho k_2 g(u,v)u}_{\mathcal{F}(u,v)} + D_u \nabla^2 u, \\ \frac{\partial v}{\partial t} = k_d u - f(u)v + \rho k_2 g(u,v)u + D_v \nabla^2 v. \end{cases} \quad (1)$$

The total mass of proteins is conserved, i.e.,$\tau = \int_{\Omega} [u(x,t) + v(x,t)] d\boldsymbol{r}$ is constant (Ω is the confined space). The reaction kinetics $\mathcal{F}(u, v)$ comprise detachment, and escape processes of DNA-bounded proteins, and recruitment of free proteins by DPICs (Session 1.1 in **Supplementary Methods**).

Here, we described each term in Eq. 1:

(i) The 1st term represents that protein dissociates from DNA, which can be written as $k_d u$, where k_d is the dissociation rate constant. We assume the k_d value of p53^{4M} ΔTAD-dsDNA is equal to that of wild type p53-dsDNA, which was reported as $0.40 \pm 0.13\ s^{-1}$ in the reference (Supplementary Table 1) (*29*).

(ii) The 2nd term is the recruitment of free protein by the DPIC. This item is written as $f(u)v$, in which $f(u)$ is the recruit function (Figs. 2A(i) & 1B). $b = \tilde{b}/k_3$, and k_3 is

conversion factor from fluorescence to concentration (Supplementary Fig. 4B(vi) and **Methods**).

(iii) The 3rd term is the escape of the DNA-bound protein from the local area to the surrounding environment. Considering that the concentration, length, and sequence of DNA can change the structure of DPIC and affect the movement of DNA-bound protein, we used the parameter ρ to capture the stability effects of DNA properties here. Therefore, this item is written as $\rho g(u,v)u$, where $g(u,v)$ is the escape function (Figs. 2A(i) & 1C), and k_2 is maximal reduction of intensity per hour (Estimated from Supplementary Fig. 5D).

(iv) The 4th term describes the Brownian movement, and ∇^2 is the Laplacian operator, i.e., $\nabla^2 = \frac{\partial^2}{\partial x^2} + \frac{\partial^2}{\partial y^2}$. Our FCS experiments provide $D_v = 18.0 \pm 1.1\ \mu m^2/s$, which matches the value of $D_v = 15.4 \pm 5.6\ \mu m^2/s$ provided in the previous reference well (Supplementary Table 1) (*29*). Our previous FRAP experiments (*24*) provide $D_u = (9.2 \pm 7.4) \cdot 10^{-4}\ \mu m^2/s$ (Supplementary Fig. 2C), which is much smaller than D_v.

In the above four terms, the recruitment led to the local increase of u, while the protein dissociation and escape lead to the decrease of u. Due to the conservation of reactions, the contribution of the first three terms to the change of v is exactly the opposite of their contribution to that of u.

Dynamical model reproduces the spatiotemporal dynamics of DPICs

(i) The plateau-shaped concentration profiles and phase diagram of DPICs. We initiated the simulation with $v_0 = 25$ and $\rho = 9$ (**Methods** and Table 1). Upon reaching equilibrium, the DNA-bound proteins formed condensates (Fig. 2B(i)), with a distinct concentration boundary separating the inside and outside the DPIC (Fig. 2B(ii)). The simulation revealed a plateau-shaped concentration profile inside the condensates, closely matching the results from the droplet-like DPIC experiments (Fig. 2B(iii)-(iv)).

To further investigate, we set the initial values of v_0 and ρ as parameter gradients along the transverse and longitudinal axes respectively (Session 1.2 in **Supplementary Methods**). This allowed us to construct a phase diagram (Fig. 2C(i)). By fixing the value of ρ = 4 and varying v_0 (10, 20, 63, and 80, as indicated by the red dashed line in Fig. 2C(i)), we observed different pattern formations (Fig. 2C(i) and insets). At a low initial v_0 (10), no condensates were formed. As v_0 increased to 20 and 63, droplet-like and "pearl chain"-like condensates appeared, respectively. When v_0 was further increased to 80, condensates were no longer formed again. Our experimental phase diagram (Fig. 2C(ii)

and Supplementary Fig. 1D) exhibited similar properties. We mixed 0.6 μM of 400-bp random DNA with varying concentrations of p53^{4M} ΔTAD. At a low protein concentration (5 μM), no DPICs were formed. When the protein concentration increased to 10 μM and 20 μM, droplet-like DPICs were observed. Further increasing the protein concentration to 40 μM resulted in the formation of "pearl chain"-like DPICs.

(ii) Spatiotemporal scale-invariance of DPICs. To further understand the spatiotemporal self-organized patterns of DPICs, we analyzed the temporal evolution of the spatial wavelength of DPIC patterns from our experiments (Fig. 3A, D, and Session 1.3 in **Supplementary Methods**). This analysis provides two key parameters: (i) Spatial scales ℓ, characterized by the time-dependent average wavelength $\ell = 2\pi L/q_{max}$ (where L represents the window size, determined using a moving window method); (ii) Dominant wavenumbers $q_{max}(t) = \int qS(q,t)\,dq / \int S(q,t)dq$, where q represents the wavenumber and $S(q,t)$ is the dynamic structure factor (*30, 31*). For stationary patterns, which can be described by the Turing principle, their spatial scales and dominant wavenumbers remain constant over time (*10*). However, for patterns exhibiting coarsening behaviors, both the spatial scales and dominant wavenumbers follow a power-law relation.

We mixed 0.3 μM of 400-bp random DNA with 10 μM p53^{4M} ΔTAD and observed the dynamical behaviors over a two-hour period (Fig. 3A(i) and Supplementary Movie 1). The experimental video demonstrated that both spatial scales and dominant wavenumbers (Session 1.3 in **Supplementary Methods**) are time-dependent. Interestingly, the spatial scales follow a power-law relation scale $\ell \propto t^m$, and the dominant wavenumbers follow $q_{max} \propto t^{-n}$ (Fig. 3A(ii)-(iii)). These results indicate that DPICs exhibit spatiotemporal scale-invariance. Specifically, the exponential factor m for the spatial scales was approximately 0.37, while for the dominant wavenumbers, n was approximately 0.26 (Fig. 3A(ii)-(iii)). To further validate our findings, we selected a model condition with $v_0 = 20$ and $\rho = 4$ from the phase diagram (Fig. 3B(i)) and performed numerical simulations of the coarsening behaviors (Fig. 3B(ii) and Supplementary Movie 2). The simulation results showed an exponential factor $m = 0.31$ for the spatial scales and $n = 0.29$ for the dominant wavenumbers (Fig. 3B(v)-(vi)). These results demonstrate that our dynamical model successfully reproduces the spatiotemporal scaling dynamics of DPICs. Unlike stationary Turing patterns, DPICs exhibit a dynamic spatiotemporal scaling behavior.

To investigate whether we can predict the trend of the exponential factor of the dominant wavenumbers under different model conditions, we selected a pathway in the phase diagram. This pathway transitions from an initial condition of $v_0 = 20$ and $\rho = 4$ to $v_0 = 25$ and $\rho = 15$, and finally to $v_0 = 30$ and $\rho = 22.5$ (Fig. 3B(i)). The coarsening behaviors along this pathway were simulated (Fig. 3B(iii)-(iv) and Supplementary Movies

3-4). We observed that the exponential factor m of the spatial scales decreased from 0.31 to 0.23, and then to 0.22, and the exponential factor n of the dominant wavenumbers decreased from 0.29 to 0.23, and then to 0.21 (Fig. 3B(vii)-(viii)). To confirm this prediction experimentally, we chose a pathway with a similar direction in the phase diagram (Fig. 3C and Supplementary Fig. 1D). Starting from the condition of 0.3 μM 400-bp random DNA with 10 μM p53^{4M} ΔTAD, we moved to 0.6 μM 400-bp random DNA with 20 μM p53^{4M} ΔTAD (Fig. 3D(i) and Supplementary Movie 5). the exponential factor m of the spatial scales decreased from 0.37 to 0.10, and the exponential factor n of the dominant wavenumbers decreased from 0.26 to 0.13 (Fig. 3D(ii)-(iii)), which aligns well with the predictions from our dynamical model.

Taken together, our dynamical model successfully reproduces the plateau-shaped concentration profiles, phase diagram, and spatiotemporal scale invariance of DPICs. These results demonstrate that mass-conserving dynamical models, previously applied to understanding animal and pebble aggregations, can also elucidate the mechanisms underlying DPIC formation. Thus, both mesoscale biomolecular condensates and macroscale biogeomorphological systems can be understood as cross-scale spatiotemporal self-organized patterns with coarsening behaviors through a unified mass-conserving reaction-diffusion model.

Dispersion relation analysis reveals that DPICs exhibit a phase-separation behavior

As previous studies (*8, 9, 32*) have demonstrated that animal and pebble aggregations exhibit phase separation behaviors, we next investigated whether DPICs also display similar phase separation characteristics.

We performed a two-dimensional (2D) spectral decomposition of our experimental DPIC patterns (Fig. 3A(i) and Supplementary Movie 1) to isolate the contribution of individual wavelengths (or wavenumbers) to the overall coarsening patterns (Session 1.5 in **Supplementary Methods**). We selected three specific wavelengths—$\lambda = 578.0\ \mu\mathrm{m}$, $60.9\ \mu\mathrm{m}$, and $17.0\ \mu\mathrm{m}$—as examples, where $\lambda = 2\pi/q$. By focusing on a time window from 300 seconds to 700 seconds, which corresponds to the early stage of the 7,200-second experimental video (Supplementary Movie 1), we observed that the calculated amplitude (Session 1.5 in **Supplementary Methods**) varies exponentially with time (Fig. 4A(i)-(iii)). The slope of the logarithmic amplitude versus time indicates the growth rate $\sigma(q)$ of the selected wavenumber q. We then plotted the growth rate $\sigma(q)$ as a function of each wavenumber q, obtaining the dispersion relation (the blue data points in Fig. 4B). Notably,

the experimental dispersion relation started from a positive value when the value of q was small.

We next asked whether our established mass-conserving dynamical model can theoretically predict our experimental dispersion relation. For this purpose, we interrogate the stability of the homogeneous steady state of Eq. 4 (**Methods**) with respect to wave-like perturbations through standard linear stability analysis, by linearizing Eq. 4 around this steady state. Every perturbation can be represented as a linear combination of Fourier modes, which initially evolve independently from each other. Linearizing and taking a Fourier transform ($u = \bar{u} + \hat{u}e^{\sigma t + i\boldsymbol{q}\vec{r}}$, $v = \bar{v} + \hat{v}e^{\sigma t + i\boldsymbol{q}\vec{r}}$) (Session 1.4 in **Supplementary Methods**), we obtain the characteristic equation

$$\sigma\binom{\hat{u}}{\hat{v}} = \begin{pmatrix} \mathcal{F}_u - \delta q^2 & \mathcal{F}_v \\ -\mathcal{F}_u & -\mathcal{F}_v - q^2 \end{pmatrix}\binom{\hat{u}}{\hat{v}} \stackrel{\text{def}}{=} A\binom{\hat{u}}{\hat{v}}, \tag{2}$$

where σ is temporal frequency and $\boldsymbol{q} = (q_x, q_y)$ is the wave vector, which can also be expressed in terms of the perturbation wavelength $\lambda = 2\pi/q$ with $q = \sqrt{q_x^2 + q_y^2}$. Self-organized patterns occur for wavenumber $q > 0$ with positive real part of $\sigma(q)$. In this case, as expected, the most unstable perturbations are the fixed undulations at the scale of $q = \sqrt{q_x^2 + q_y^2}$ with the maximum growth rate $\Re e[\sigma(q)]$, where

$$\sigma_{1,2}(\mathrm{q}) = \frac{1}{2}\mathrm{tr}(A) \pm \frac{1}{2}\sqrt{\mathrm{tr}(A)^2 - 4\det(A)} \tag{3}$$

Eq. 3 provides the theoretical dispersion relation for the model described by Eq. 4, illustrating the initial rate of growth or decay of perturbations with various wavenumbers (Session 1.6 in **Supplementary Methods**). From Fig. 3, we determined that the experimental condition (0.3 μM 400-bp random DNA with 10 μM p53^{4M} ΔTAD) corresponds to a model condition with $u_0 = 0.5$, $v_0 = 20$ and $\rho = 4$ in the phase diagram (Fig. 3B(i)). Using these data, we plotted the theoretical dispersion relation $\Re e[\sigma(q)]$ as a function of wavenumber q based on Eq. 3 with $\bar{u} = 16.6$ and $\bar{v} = 3.9$ (the red solid line in Fig. 4B), which aligns well with the experimental data (the blue data points in Fig. 4B). In addition, the dispersion relation of the model condition started from a positive value when q is close to 0, indicating that our DPICs are not Turing patterns. The reason is that classical Turing theory predicts that the dispersion relation of Turing patterns starts from a negative value at wavenumber $q = 0$ (*4, 10, 33, 34*).

To investigate whether we could predict the trend of the dispersion relation, we adjusted the model condition to $u_0 = 0.5$, $v_0 = 37.3$ and $\rho = 16$ in the phase diagram (Fig. 3B(i)). The theoretical prediction for this condition (represented by the brown solid line) is

plotted in Fig. 4B based on Eq. 3 with $\bar{u} = 35.1$ and $\bar{v} = 2.7$. Considering the total protein concentration ($\bar{u} + \bar{v}$) was increased from 20.5 to 37.8, to experimentally confirm this prediction, we selected an experimental condition of 0.6 μM 400-bp random DNA with 20 μM p53^{4M} ΔTAD (Fig. 3D(i) and Supplementary Movie 5), which corresponds to a similar direction of increased total mass of protein with the model condition in the phase diagram (Fig. 3C). Comparing the theoretical dispersion relation with the experimental data (represented by the orange dots in Fig. 4B), we observed that the experimental data exhibited the same characteristic shape as the theoretical prediction.

Taken together, our findings reveal that DPICs exhibit a specific dispersion relation distinct from that of typical Turing patterns. Furthermore, our analysis demonstrated that DPICs form spatiotemporal self-organized patterns with coarsening behaviors. These conclusions collectively provide compelling evidence that DPICs exhibit phase-separation behaviors.

DPICs exhibit emergent properties

When we analyzed the dominant wavenumbers q_{max} (Session 1.3 in **Supplementary Methods**) for the phase separation system of 0.3 μM 400-bp random DNA and 10 μM p53^{4M} ΔTAD (Fig. 3A(i) and Supplementary Movie 1), we discovered a notable result. By plotting $S(q,t)q_{max}^2$, defined as the structure function, versus rescaled q/q_{max} at various time points (1,290, 2,790, 4,290, 5,790, and 7,290 seconds), we observed that each structure function follows a power-law relation. Remarkably, all data points collapsed onto a single universal master line, with an exponential factor of -4.1 (Fig. 5A(i)). Furthermore, a different experimental condition of 0.6 μM 400-bp random DNA and 20 μM p53^{4M} ΔTAD (Fig. 3D(i) and Supplementary Movie 5) has the same exponential factor of -4.1 (Fig. 5A(ii)). When we repeated this analysis for two different numerical simulations in the phase diagram (Fig. 3B(i)), $v_0 = 20$ and $\rho = 4$; $v_0 = 30$ and $\rho = 22.5$, we obtained the same exponential factor of -4.6 (Fig. 5B(i)-(ii)). We observed a slight discrepancy between the experimental and theoretical exponential factors, which can be attributed to Porod's Law (*35*).

These findings quantitatively indicate that our DPICs exhibit emergent properties (*36*). The clear power-law scaling also rules out any significant effects due to finite system size, akin to the behaviors observed in classical sandpiles (*37-39*) and forest fire systems (*40, 41*).

Discussion

In this study, we successfully conducted a quantitative analysis of a specific type of mesoscale biomolecular condensate, known as DPICs, by establishing a mass-conserving dynamical models. Our findings reveal that our DPICs exhibit spatiotemporal self-organized patterns with coarsening behaviors (Fig. 2-3), phase separation behavior (Fig. 4), and emergent properties (Fig. 5). We wish to emphasize two key points: (i) DPICs are ideal candidates for model development because they are mass-conserved and contain a recruitment function $f(u)$ that reflects positive feedback and an escape function $g(u,v)$ that reflects negative feedback. We propose that any mass-conserved biomolecular condensate system with both positive and negative local concentration-dependent feedback mechanisms can be successfully quantitatively analyzed using a similar type of mass-conserving dynamical models; (ii) Unlike previous studies (*10, 27, 42, 43*), all parameters in our dynamical model (Supplementary Table 1) were derived from direct experimental measurements.

Based on our data, several interesting topics warrant further exploration in future studies. One key area is the investigation of mass-conserving dynamical models. These models are sufficient to generate coarsening patterns, unlike Turing patterns, which possess only one characteristic length scale (*33, 44*). Interestingly, similar mass-conserving dynamical models have previously been applied to macroscale biogeomorphological systems (*8, 9, 45, 46*). Both mesoscale biomolecular condensates and macroscale biogeomorphological systems exhibit cross-scale spatiotemporal self-organized patterns with coarsening behaviors and phase separation behavior, along with emergent properties. Therefore, mass-conserving dynamical models provide an ideal cross-scale paradigm for studying pattern formation in mass-conserved systems with coarsening behaviors. This area warrants further quantitative investigation from both experimental and mathematical perspectives.

Second is about non-mass-conserving systems. It is well known that natural systems more commonly exhibit non-mass-conserving dynamics than mass-conserving ones. Here, we hypothesize that a mass-conserving model can approximate a real, complex non-mass-conserving system under specific conditions. This hypothesis has been successfully utilized by Frey and colleagues to understand cell polarity aggregation (*25, 27*). Future studies should investigate the applicability of mass-conserving models as approximations for non-mass-conserving systems, which could provide significant insights into the dynamics of various natural phenomena.

Thirdly, we demonstrate phase-separation behavior. Both the Turing principle (*1, 2, 4, 26*) and the phase separation principle (*12, 13, 47*) can be used to study self-organized patterns. However, distinguishing between Turing patterns and phase-separation

patterns is challenging due to their spatial similarities. Here, we propose a new method to identify phase-separation behavior in patterns. This method involves two investigations: (i) Investigating whether the patterns exhibit coarsening behavior. If the spatial scales and dominant wavenumbers of a pattern (Session 1.3 in **Supplementary Methods**) follow a power-law relation, the pattern demonstrates coarsening behavior; (ii) Investigating the dispersion relation of a pattern (Session 1.5 in **Supplementary Methods**). The dispersion relation for Turing patterns begins with a negative value at wavenumber $q = 0$. Therefore, if the dispersion relation of a pattern starts from a positive value when q is close to 0, the pattern is not a Turing pattern. We propose that when a pattern exhibits both coarsening behavior and a non-Turing dispersion relation, it can be identified as demonstrating phase-separation behavior.

Our study demonstrates that DPICs form spatiotemporal self-organized patterns with coarsening behaviors (Fig. 3). Additionally, the dispersion relations for both experimental and theoretical DPIC start from a positive value at wavenumber q is close to 0 (Fig. 4). Thus, we establish that DPICs exhibit phase-separation behaviors. To our knowledge, these experiments and theoretical predictions provide the first coherent evidence for phase separation frameworks through the approach of dispersion relation. Alongside the scaling-invariance coarsening behaviors of the pattern, this evidence clearly differentiates phase separation from classical Turing instability in pattern formation. Developing new methods to demonstrate phase-separation behaviors could provide crucial insights into whether various types of biomolecular condensates in living cells exhibit phase-separation behaviors. This presents another fascinating topic for future research.

Fourth is about spatiotemporal scale-invariance. In Fig. 3, the spatial scales of DPICs follow a power-law relation, $\ell \propto t^m$, demonstrating spatiotemporal scale-invariance. Remarkably, each well-studied system of animal and pebble aggregations, characterized by a unique coarsening exponent m, can be associated with a biomolecular condensate system exhibiting a similar coarsening exponent (Fig. 6). For instance, both macroscale mussel beds (*9*) and mesoscale nucleolar protein FIB-1 condensates in living cells (*48*) share a coarsening exponent of $m \sim \frac{1}{3}$; macroscale stone patterns (*8*) and mesoscale DPICs in our experiments (*24*) both exhibit $m \sim \frac{1}{4}$; and both macroscale dunes and ripples (*49*)) and mesoscale chromatin-protein condensates in living cells (*50-52*) have coarsening exponents $m < \frac{1}{5}$. This high degree of consistency suggests a compelling idea: mesoscale biomolecular condensates could serve as model systems for studying macroscale biogeomorphological systems, akin to how Drosophila (fruit fly) and Caenorhabditis (nematode worm) are used to model human diseases. This is another interesting topic for the future study.

In addition to macroscale animal and pebble aggregations (ranging from meters to kilometers) and mesoscale biomolecular condensates (ranging from nanometers to micrometers), recent research (*7*) has demonstrated that the aggregation of living T. tubifex worms (centimeter scale) also exhibits similar phase-separation behavior. We hypothesize that this system may follow the same mass-conserving dynamical model. If confirmed, the applicability of the similar type of mass-conserving dynamical models could extend across scales from nanometers to kilometers. This presents another fascinating topic for future research.

In summary, our findings establish a cross-scale bridge connecting mesoscale biomolecular condensates within living cells and macroscale biogeomorphological systems using a unified mass-conserving dynamical model. These insights enhance our understanding of the mechanisms underlying spatiotemporal self-organized patterns with coarsening behaviors, and phase separation across vastly different scales.

Acknowledgments

We thank the Peking Nanofab for process support. We thank the contributions of the Engineering Research Center for Semiconductor Integrated Technology, Institute of Semiconductors, Chinese Academy of Sciences. We thank Dr. Chunlai Chen for help us to conduct FCS experiments. We thank all members of the Qi laboratories for comments on the manuscript.

Author Contributions

C.L. prepared biological samples, conducted all experiments, performed data analysis, and wrote the manuscript. M.T.G. and X.Q.H. performed simulation and theoretical analysis, and X.Q.H., and Q.X.L. built up the theoretical model. Z.Q., Q.X.L., and X.Q.H. supervised the project, experimental designs, and data analysis, and wrote the manuscript with input from all authors.

Funding

This work was supported by National Natural Science Foundation of China (Grant No. T2225009 (Z.Q.), T2321001, 32088101, 32071609 (Q.X.L.), 12071141 (X.Q.H.)), and Science and Technology Commission of Shanghai Municipality (No. 22DZ2229014).

Figures

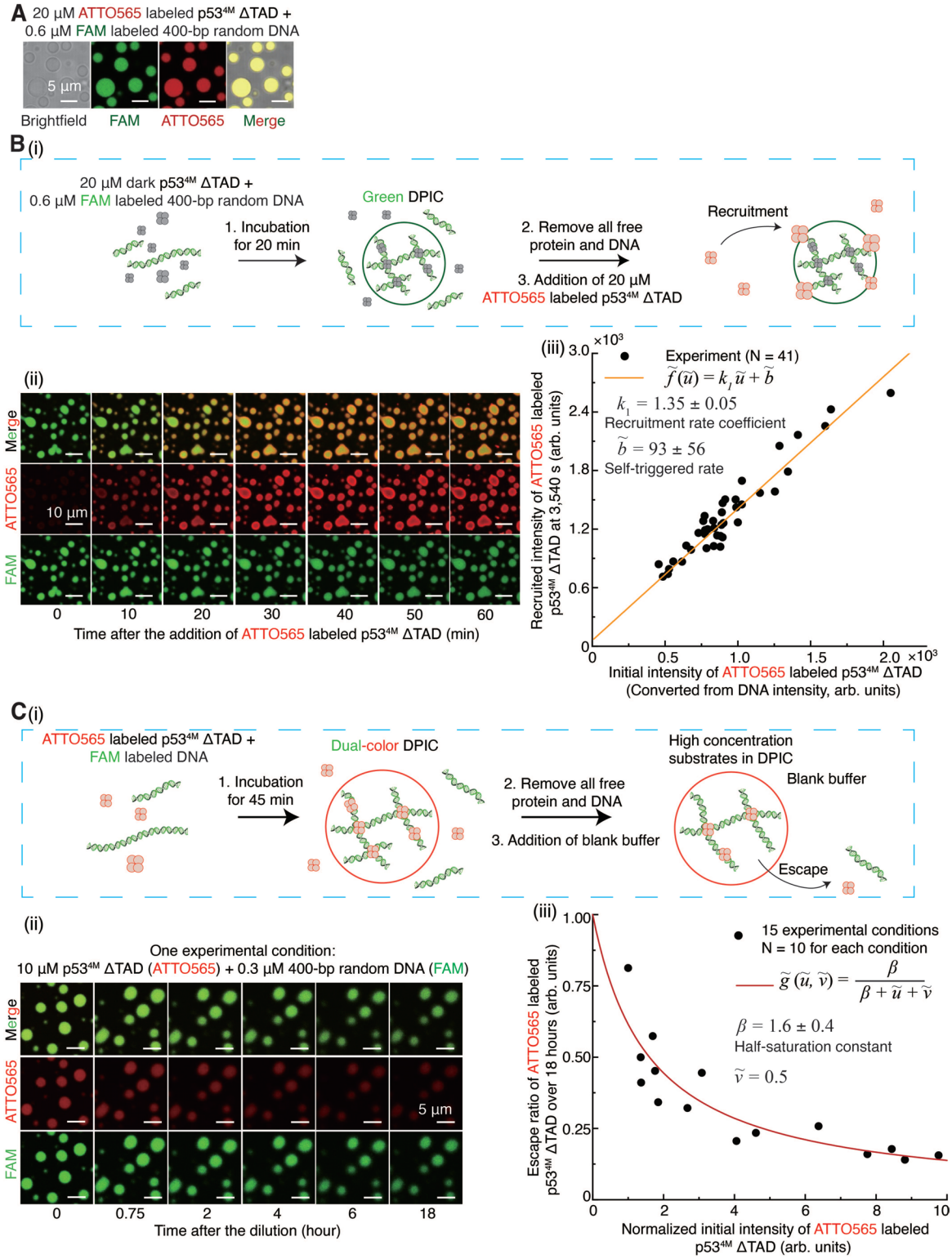
A 20 μM ATTO565 labeled p53⁴ᴹ ΔTAD +
0.6 μM FAM labeled 400-bp random DNA
5 μm
Brightfield
FAM
ATTO565
Merge
B (i)
20 μM dark p53⁴ᴹ ΔTAD +
0.6 μM FAM labeled 400-bp random DNA
1. Incubation for 20 min
Green DPIC
2. Remove all free protein and DNA
3. Addition of 20 μM ATTO565 labeled p53⁴ᴹ ΔTAD
Recruitment
(ii)
Merge
ATTO565
FAM
10 μm
0
10
20
30
40
50
60
Time after the addition of ATTO565 labeled p53⁴ᴹ ΔTAD (min)
(iii)
×10³
Experiment (N = 41)
$\tilde{f}(\tilde{u}) = k_1 \tilde{u} + \tilde{b}$
$k_1 = 1.35 \pm 0.05$
Recruitment rate coefficient
$\tilde{b} = 93 \pm 56$
Self-triggered rate
Recruited intensity of ATTO565 labeled p53⁴ᴹ ΔTAD at 3,540 s (arb. units)
Initial intensity of ATTO565 labeled p53⁴ᴹ ΔTAD
(Converted from DNA intensity, arb. units)
C (i)
ATTO565 labeled p53⁴ᴹ ΔTAD +
FAM labeled DNA
1. Incubation for 45 min
Dual-color DPIC
2. Remove all free protein and DNA
3. Addition of blank buffer
High concentration substrates in DPIC
Blank buffer
Escape
(ii)
One experimental condition:
10 μM p53⁴ᴹ ΔTAD (ATTO565) + 0.3 μM 400-bp random DNA (FAM)
Merge
ATTO565
FAM
5 μm
0
0.75
2
4
6
18
Time after the dilution (hour)
(iii)
15 experimental conditions
N = 10 for each condition
$\tilde{g}(\tilde{u}, \tilde{v}) = \frac{\beta}{\beta + \tilde{u} + \tilde{v}}$
$\beta = 1.6 \pm 0.4$
Half-saturation constant
$\tilde{v} = 0.5$
Escape ratio of ATTO565 labeled p53⁴ᴹ ΔTAD over 18 hours (arb. units)
Normalized initial intensity of ATTO565 labeled p53⁴ᴹ ΔTAD (arb. units)

Fig. 1 DPICs exhibit both positive and negative local concentration-dependent dynamic behaviors of proteins. (**A**) Two-color *in vitro* droplet assays involving the mixing of 0.6 μM 400-bp random DNA labeled by FAM with 20 μM $p53^{4M}$ ΔTAD labeled by ATTO565. (**B**) (i) Schematic of the designed "recruitment experiment". (ii) Time course of the recruitment of free protein into the two color-labeled DPICs, with time indicated in minutes. (iii) The intensity of recruited ATTO565-labeled $p53^{4M}$ ΔTAD at equilibrium versus the initial amount of $p53^{4M}$ ΔTAD inside the DPIC (Supplementary Fig. 4B(v)) was plotted, which can be fitted by a recruitment function, $\tilde{f}(\tilde{u}) = k_1\tilde{u} + \tilde{b}$. (**C**) (i) Schematic of the designed "escape experiment". (ii) Time course of the escaped protein from the two color-labeled DPICs, with time indicated in minutes. Here is one specific experimental condition of 10 μM $p53^{4M}$ ΔTAD labeled with ATTO565 and 0.3 μM 400-bp random DNA labeled with FAM. All data of 15 different experimental conditions were shown in Supplementary Fig. 5. (iii) The escape ratio of proteins at the 18-hour time point versus the normalized initial amount of $p53^{4M}$ ΔTAD inside DPIC at 0-hour time point was plotted, which can be fitted by a escape function, $\tilde{g}\,(\tilde{u}, \tilde{v}) = \frac{\beta}{\beta+\tilde{u}+\tilde{v}}$. Independent *in vitro* droplet experiments in a, b(ii), and c(ii) were conducted three times (n = 3). It is pertinent to note that in the subsequent sections, mathematical symbols with a tilde denote the fluorescent intensity measured from experiments, whereas symbols without a tilde represent concentration.

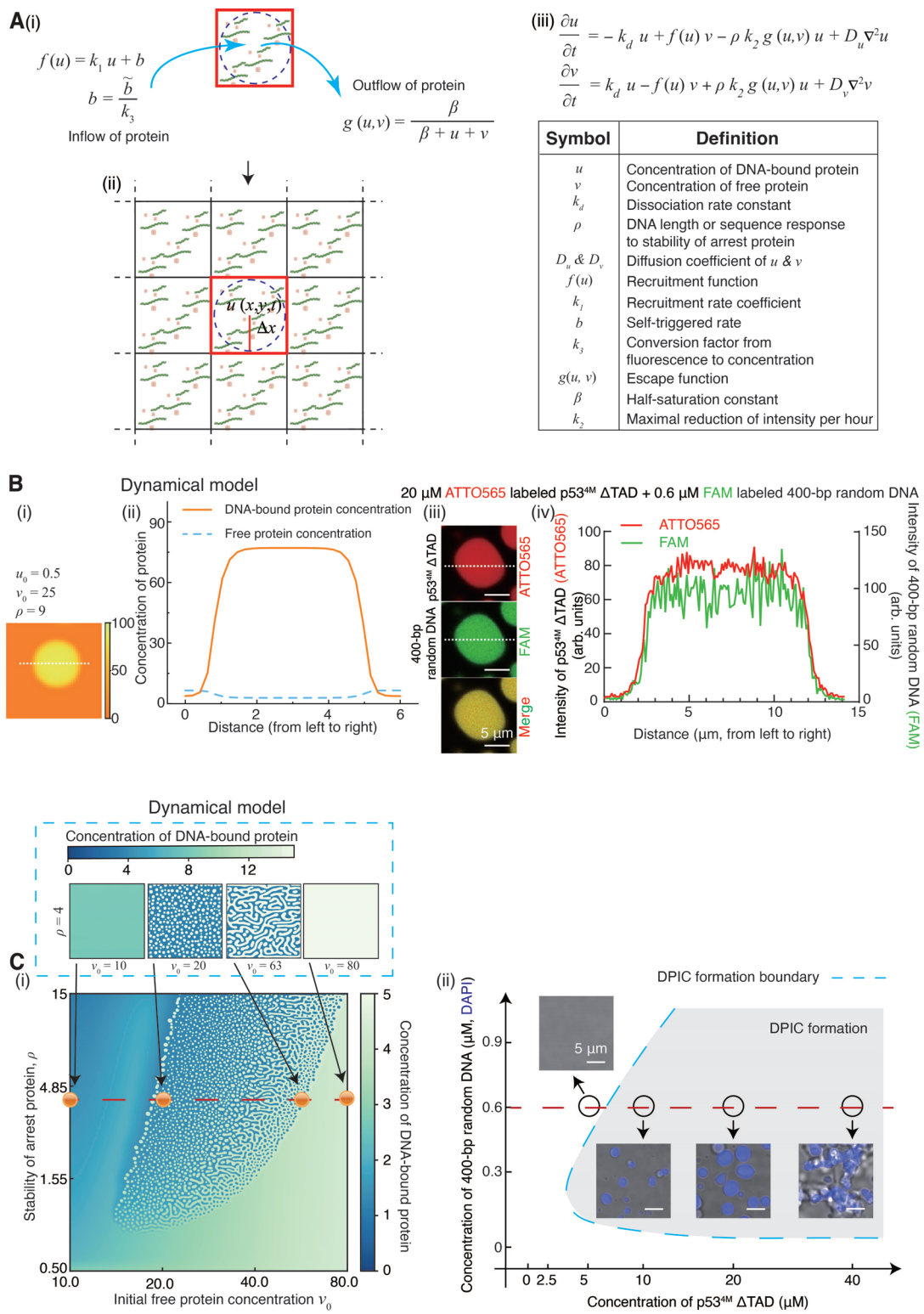

Fig. 2 A mass-conserving dynamical model successfully reproduced the spatiotemporal dynamics of DPICs. (**A**) A mass-conserving dynamical model was established. (i) A diagram illustrating the kinetic processes of recruitment and escape at

space (x, y) within a Δt time interval; (ii) Each spatial lattice point is associated with the protein-DNA interactions that are analogous to a spatially homogeneous system; (iii) The mass-conserving dynamical model. All symbol definitions were in the table (Supplementary Table 1 and **Supplementary Methods**). (**B**) (i) A simulated droplet-like DPIC by a numerical simulation with $u_0 = 0.5$, $v_0 = 25$, $\rho = 0.5$, $D_v = 0.17$, $D_u = 0.05D_v$; (ii) The simulated DPIC profiles for DNA-bound protein (u) and free protein (v) in (i) showed a plateau shape; (iii) A experimental droplet-like DPIC by a two-color *in vitro* droplet assay involving the mixing of 0.6 μM 400-bp random DNA labeled by FAM with 20 μM $p53^{4M}$ ΔTAD labeled by ATTO565; (iv) The experimental phase-separation profile in (iii) also showed a plateau shape. (**C**) (i) Model-predicted phase diagram, which was plotted in the plane of v_0 and ρ. (*Insets*) Model-predicted spatial patterns following a red dashed line by fixing the value of ρ = 4 and varying v_0 (10, 20, 63, and 80); (ii) Experimental phase diagram, which was plotted in the plane of concentrations of $p53^{4M}$ ΔTAD and concentration of 400-bp random DNA. (*Insets*) Experimental spatial patterns following a red dashed line by fixing the value of 0.6 μM 400-bp random DNA and varying $p53^{4M}$ ΔTAD concentrations (5, 10, 20, and 40 μM).

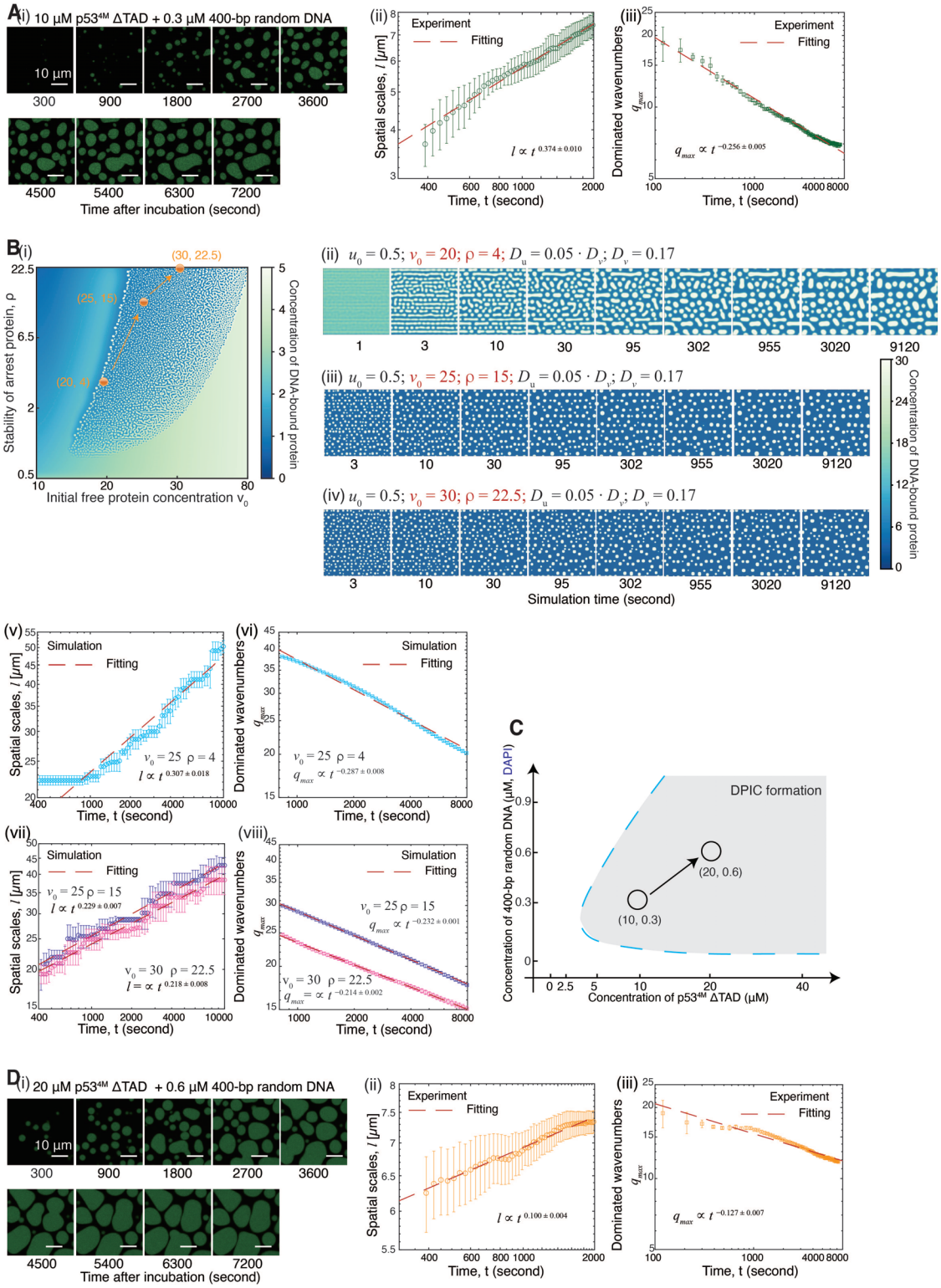

Fig. 3 Spatiotemporal scale-invariance of DPICs from experiments and numerical simulations. (**A and D**) Spatiotemporal dynamics of DPICs formed by 0.3 μM 400-bp random DNA labeled by FAM with 10 μM dark p53^{4M} ΔTAD (A), or 0.6 μM 400-bp random

DNA labeled by FAM with 20 μM dark p53^{4M} ΔTAD (D). (i) Time course of coarsening behavior of DPICs, with time indicated in minutes; (ii) Spatial scales ℓ over time; (iii) Dominant wavenumbers q_{max} over time. Independent analysis was repeated: N = 5 for 5 different observation regions in one experiment. Both the spatial scales and dominant wavenumbers follow power-law relations (The dashed line in (ii)-(iii) represents the power-law fitting). Error bars, mean ± s.d. (**B**) Spatiotemporal dynamics of simulated DPICs. (i) Model-predicted phase diagram, which was plotted in the plane of v_0 and ρ. (ii)-(iv) Simulation time course of coarsening behavior of DPICs for three different model conditions, with simulation time indicated in minutes: (ii) $u_0 = 0.5$, $v_0 = 20$, $\rho = 4.0$, $D_v = 0.17$, $D_u = 0.05D_v$; (iii) $u_0 = 0.5$, $v_0 = 25$, $\rho = 15$, $D_v = 0.17$, $D_u = 0.05D_v$; (iv) $u_0 = 0.5$, $v_0 = 30$, $\rho = 22.5$, $D_v = 0.17$, $D_u = 0.05D_v$. The color bar represents the concentration of DNA-bounded protein. The direction of the pathway for these three different model conditions is upper right. (v)-(viii) Spatial scales ℓ and dominant wavenumbers q_{max} over time. (v)-(vi) for model condition (ii); (vii)-(viii) for model condition (iii)-(iv). Independent simulations were repeated 5 time (n = 5) for (ii)-(iv). Error bars, mean ± s.d. (**C**) Experimental phase diagram (Fig. 2C(ii) and Supplementary Fig. 1D). The direction of the pathway for these two different experimental conditions is also upper right.

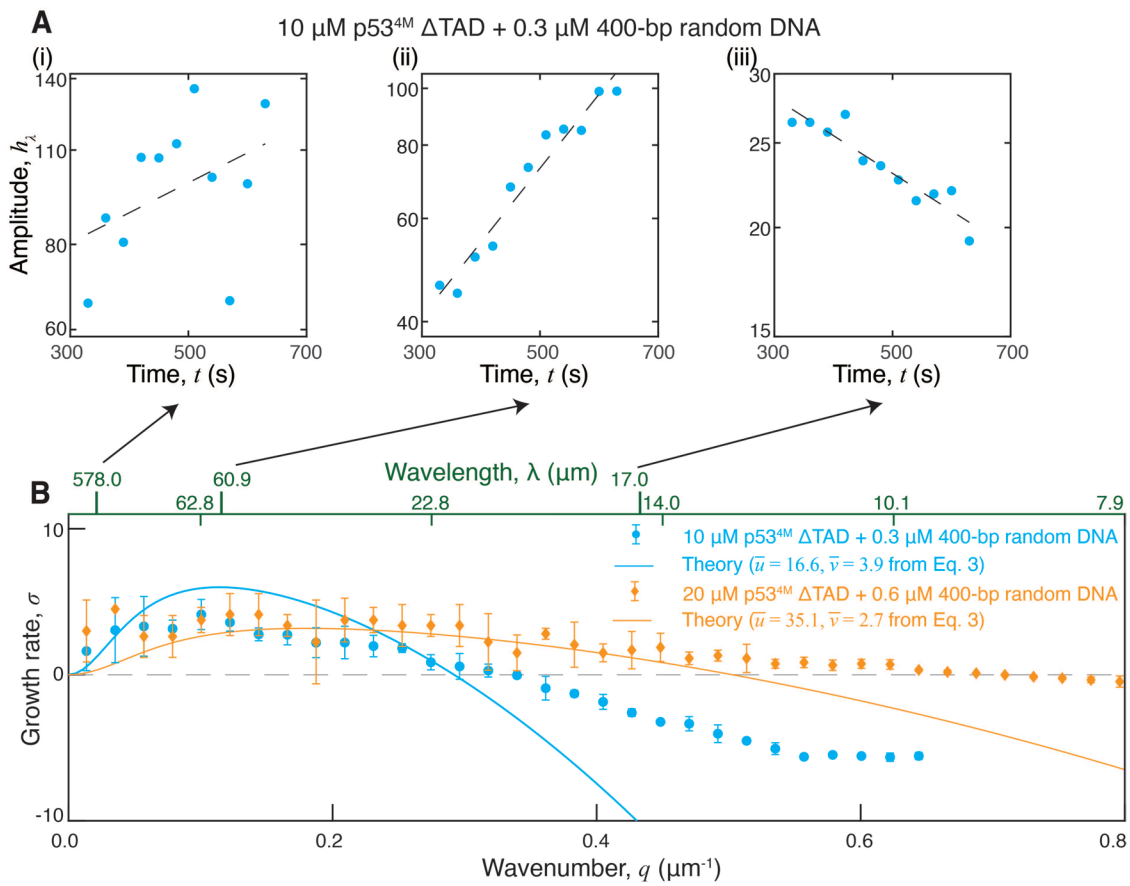

Fig. 4 The dispersion relation of p53 DPIC from experiments and theoretical predictions. (**A**) For the DPICs of 0.3 μM 400-bp random DNA with 10 μM dark p53^{4M} ΔTAD, amplitude versus time (300-700 seconds, the early stage of the 7,200-second experimental video) for three specific wavelengths—$\lambda = 578.0\ \mu\text{m}$ (i), $60.9\ \mu\text{m}$ (ii), and $17.0\ \mu\text{m}$ (iii)—as examples, where $\lambda = 2\pi/q$. The slope of the logarithmic amplitude varies exponentially with time (the black dashed line in (i)-(iii)) indicates the growth rate $\sigma(q)$ of the selected wavenumber q. (**B**) The growth rate $\sigma(q)$ versus wavenumber q (and wavelength λ). Experimental condition 1 (blue circle): 0.3 μM 400-bp random DNA with 10 μM dark p53^{4M} ΔTAD; Model condition 1 (red line): $\bar{u} = 16.6$, $\bar{v} = 3.9$, $\rho = 4.0$, $\delta = 0.003$; Experimental condition 2 (orange circle): 0.6 μM 400-bp random DNA with 20 μM dark p53^{4M} ΔTAD; Model condition 2 (brown line): $\bar{u} = 35.1$, $\bar{v} = 2.7$, $\rho = 16.0$, $\delta = 0.0005$. The direction of the pathway from Experimental condition 1 to Experimental condition 2 in the phase diagram is the same as from Model condition 1 to Model condition 2. Error bars, mean ± s.d.

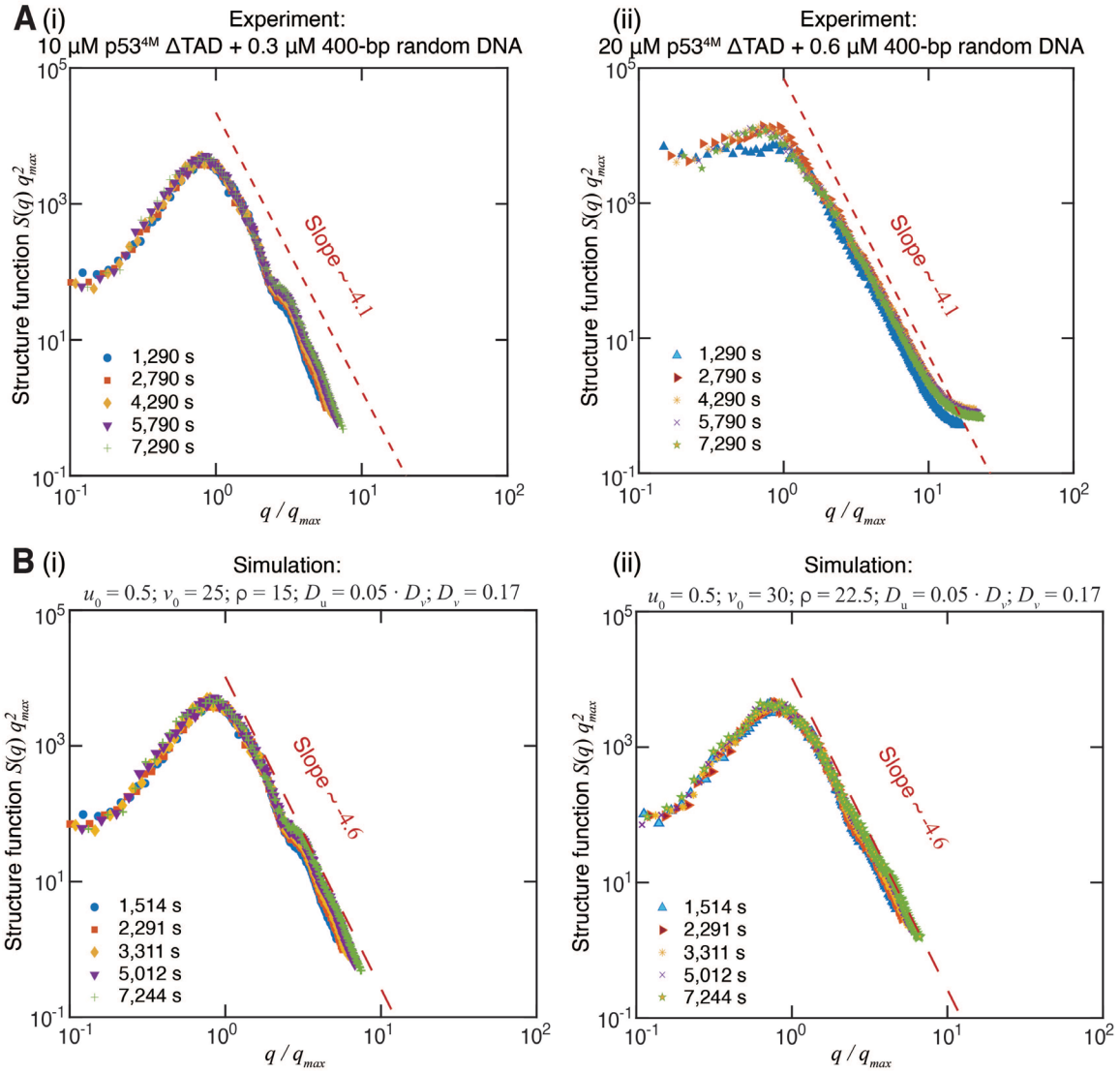

Fig. 5 Emergent properties of the self-organized scale of p53 DPICs from experiments and numerical simulations. (**A**) The experimental data were plotted as the rescaled structure function $S(q)q_{max}^2$ versus q/q_{max} at various time points (1,290, 2,790, 4,290, 5,790, and 7,290 seconds). All points collapse onto one single power-law line (dashed red lines) with a same slope ~-4.1. (i) The experimental condition: 10 μM p53^{4M} ΔTAD mixed with 0.3 μM 400-bp random DNA; (ii) The experimental condition: 20 μM p53^{4M} ΔTAD mixed with 0.6 μM 400-bp random DNA. (**B**) (i)-(ii) We used two different model conditions to conduct numerical simulations, repeating the analysis in (A). The rescaled structure factors collapse to form a master line all with the same slope ~-4.6.

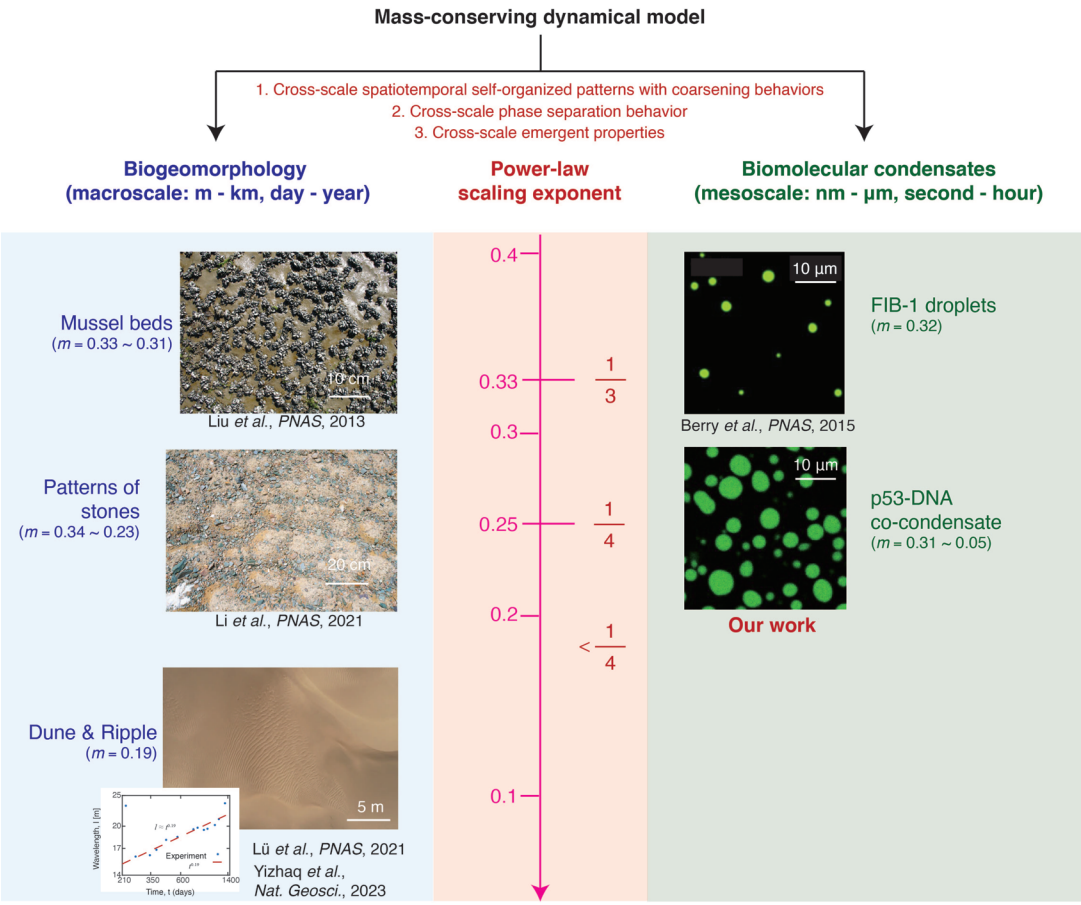

Fig. 6 A mass-conserving dynamical model for systems across scales. According to the power-law scaling exponent observed during coarsening behavior, a straightforward correlation can be established between macroscale biogeomorphological systems and mesoscale biomolecular condensates.

Tables

Table 1. Scaled parameter interpretations, default values, and their definitions.

Symbol	Interpretation	Scaled parameter definition	Default value
$\boldsymbol{T}$	Dimensionless time	$T = k_d t$	
$\boldsymbol{\beta_1}$	Scaled recruitment rate coefficient	$\beta_1 = \frac{k_1}{k_d}$	3.75
$\boldsymbol{b_1}$	Scaled constant reaction rate	$b_1 = \frac{b}{k_d}$	25.0
$\boldsymbol{\beta_2}$	Scaled escape rate	$\beta_2 = \frac{k_2 \beta}{k_d}$	100
$\boldsymbol{\delta}$	Ratio of diffusion coefficients between u and v	$\delta = \frac{D_u}{D_v}$	$\mathcal{O}(10^{-2} \sim 10^{-4})$
$\boldsymbol{X}$	Scaled spatial length	$X = k_d^{\frac{1}{2}} D_v^{\frac{-1}{2}} x$	102.4
$\boldsymbol{k_d}$	Dissociation rate		1.0
$\boldsymbol{\beta}$	Half-saturation constant	β	2.0
$\boldsymbol{\rho}$	DNA length or sequence response to stability of arrest protein	ρ	5.0
$\boldsymbol{U}$	Concentration of DNA-bound protein		
$\boldsymbol{V}$	Concentration of free protein		

Methods

Construction of bacterial expression plasmids, protein purification and protein labeling

It has been proved that the TAD truncated p53 which contains 4 mutations (M133L/V203A/N239Y/N268D), called $p53^{4M}$ ΔTAD, can form DPIC with dsDNA in *in vitro* droplet assays (*24*). We cloned $p53^{4M}$ ΔTAD on the pRSFDuet vector and inserted a 6× His-tag to construct the expression plasmid. The sequence of 6× His-$p53^{4M}$ ΔTAD was shown in the supplementary table.

The protein expression plasmid was transformed to *E. coli* strain BL21(DE3), and then cultured overnight on LB agar plates at 37 °C. One single clone of bacteria was cultured overnight in 10 mL LB medium at 37 °C and 220 rpm. The culture was added into a 2 L LB medium and grew to the density OD_{600} of 0.6. The bacteria were induced to express protein by the addition of 0.3 mM IPTG and 0.1 mM $ZnCl_2$, and then cultured at 16 °C and 180 rpm for 18 h. The culture was centrifuged with 4,000× g. Cells were resuspended in a lysis buffer (25 mM Tris-HCl (pH 7.5), 500 mM NaCl, 5 mM imidazole, 0.25‰ β-Mercaptoethanol (β-Me), and 5% Glycerol) with 1 mM PMSF, and then sonicated on ice. The supernatant was separated and filtered after centrifugation at 18,000× rpm for 30 min. Ni-NTA was used to bind $p53^{4M}$ ΔTAD and then washed by a washing buffer (25 mM Tris-HCl (pH 7.5), 500 mM NaCl, 20 mM imidazole, 0.25‰ β-Me, and 5% Glycerol). The proteins were eluted with an elution buffer (25 mM Tris-HCl (pH 7.5), 500 mM NaCl, 300 mM imidazole, 0.25‰ β-Me, and 5% Glycerol), and then purified by gel filtration with a Superdex 200 increase GL 10/300 (GE Healthcare, USA) with a storage buffer (20 mM Tris-HCl (pH 7.5), 300 mM NaCl, 10% Glycerol, and 40 mM DTT). After a quick-frozen by liquid nitrogen, the proteins were stored at a -80 °C environment.

In the recruitment experiment and escape experiments, the $p53^{4M}$ ΔTAD was labeled by ATTO565 NHS ester (Sigma Cat: 72464) at 1:1.5 molar ratios in 0.1 M $NaHCO_3$ for 1 hour at 4 ^{o}C. In the FCS assay, $p53^{4M}$ ΔTAD was labeled by Sulfo Cyanine5 (Cy5) NHS ester (Lumiprobe) at 1:4 molar ratios in reaction buffer (20 mM HEPES pH 7.5, 150 mM KCl, 10% glycerol, 1 mM TCEP) and incubated for 20 min at RT. These proteins were purified by gel filtration with a Superdex 200 increase GL 10/300 with the storage buffer, and then stored at -80 °C.

Electrophoretic Mobility Shift Assay (EMSA)

EMSA was used to test the DNA-binding activity of $p53^{4M}$ ΔTAD in this paper. 30-bp DNA probes were generated by annealing DNA primers. The top strand labeled by 5'-

quasar 670 and the bottom strand with no labeling were mixed at a molar ratio of 1:1.2 in an annealing buffer (40 mM Tris-HCl (pH 8.0), 50 mM NaCl, and 10 mM $MgCl_2$). The mixture was heated to 95 °C for 5 min and then slowly cooled down to room temperature (RT) together with the heater. The concentration of 30-bp DNA probes was considered as 1 μM. The DNA sequences are shown in the supplementary table.

The DNA probes were diluted to 0.05 μM and the $p53^{4M}$ ΔTAD was diluted into different working concentrations by the p53 working buffer (20 mM HEPES (pH 7.9), 150 mM NaCl, 2 mM $MgCl_2$, 1 mM DTT, and 0.5 mg/mL BSA). The DNA probes were mixed with $p53^{4M}$ ΔTAD, incubated at RT for 30 min, and then resolved by 1% agarose gel in TBE buffer under 60 V for 90 minutes in a cold room (4 °C). The results were scanned by an Amersham Typhoon RGB system (with a 635 nm laser and Cy5 670BP30 filter).

In vitro droplet assay

The FAM-labeled 400-bp random DNA and Cy5-labeled 400-bp random DNA were obtained by polymerase chain reaction (PCR) with a template of a sequence containing no p53-specific binding sites on the genome of lambda phage. In this PCR reaction, one primer carried a FAM or Cy5 tag at the 5' terminal, and the other primer did not carry any tag. $p53^{4M}$ ΔTAD with or without ATTO565 labeling were prepared as above. The DNA and protein substrates were centrifuged at 12,000× rpm for 10 min at 4 °C and then diluted to the working concentration by ddH_2O and p53 storage buffer, respectively. All *in vitro* samples were mixed and dropped into 384-well plates (Cellvis). The DNA-protein mixture was incubated at RT in a p53 droplet buffer (8 mM Tris-HCl (pH 7.5), 120 mM NaCl, 4% Glycerol, and 16 mM DTT). Confocal (Leica TCS SP8) was used to observe the DPICs.

The raw image data were analyzed using Fiji (ImageJ Version: 2.0.0-rc-61/1.52n). Fluorescence images were initially converted to 8-bit format. The average intensity of ATTO565- or FAM-labeled components was then measured by analyzing either the entire area of the DPIC or a specific region within the DPIC, depending on the experimental requirements. As demonstrated in Supplementary Fig. 4A, there is a strong linear correlation between the average intensity of fluorescent molecules and their concentration. Therefore, the concentration of protein or DNA in the measured region can be determined by multiplying the average fluorescence intensity of ATTO565 or FAM by a conversion factor from fluorescence intensity to concentration. Since our dynamic model is two-dimensional, the total amount of the components can be determined by multiplying their concentration by the area of measured region.

For “recruitment experiment”, the ordinate is the total intensity of ATTO565 signal recruited by each DPIC at the 3,540-second time point. According to the results of Supplementary Fig. 4B, the distribution of FAM or ATTO565 of different DPICs under the same experimental condition is highly consistent, and the average intensity of ATTO565 is 0.8 times that of FAM, so the abscissa which is the initial amount of protein in DPIC is calculated by 0.8 × total FAM intensity of DPIC at 0 s. For “escape experiment”, the ordinate is the escape ratio of ATTO565 at the 18-hour time point, which is calculated by the total intensity change over 18 hour / the total intensity at 0 h. The abscissa is the rescaled total intensity of ATTO565, which is calculated by the total intensity of each condition / the minimal value.

To estimate the value of the conversion factor $\boldsymbol{k_3}$ from ATTO565 intensity to the concentration of p53^{4M} ΔTAD, we conducted the following analysis. For a mass-conserved system, the concentration of the protein and its volume fraction have the following relationship:

$$C_{ini} = C_{out} \times \varphi_{out} + C_{in} \times \varphi_{in}$$

C_{out} and C_{in} represent the protein concentration outside and inside the DPIC, respectively. φ_{out} and φ_{in} represent the volume fraction of outside and inside the DPIC, respectively. C_{ini} is the initial protein concentration, which is 20 μM in the condition of Supplementary Fig. 4B. Since the volume fraction of DPIC in the whole reaction system was small, we assumed φ_{in} was 0.4%. Then, we measured C_{in}/C_{out} of p53^{4M} ΔTAD by calculating the average ATTO565 intensity inside DPIC / that outside DPIC (Supplementary Fig. 4B(vi)). In this way, we estimated that the protein concentration inside DPIC was approximately 530 μM. Due to the average ATTO565 intensity inside DPIC was about 80 (Supplementary Fig. 4B(v)), the value of $\boldsymbol{k_3}$ was calculated by 530 / 80, which approximated to 6.7.

Fluorescence recovery after photobleaching (FRAP)

The ATTO565 labeled p53^{4M} ΔTAD and FAM labeled 400-bp random DNA were mixed and incubated for 2 hours at room temperature to obtain large DPICs. 488-nm and 561-nm lasers of a spinning-disk confocal microscope (UltraView VoX) were used to bleach an area of 1.5 μm × 1.5 μm inside DPIC with the strength of 100% for 30 cycles. The recovery process was then recorded with a speed of 2 min per frame for 120 min. A region with a radius of 1.2 μm was selected to completely cover the bleached area, which was defined as a Region Of Interest (ROI). Meanwhile, an area of the same size was selected inside DPIC without bleaching as Control. After that, the average intensity of FAM and ATTO565 in the regions of all ROIs and Controls at each time point was measured. To correct the photobleaching during the 120-minute observation, the intensity of ROI was

normalized to the intensity of control. Then, the intensity of each time point of ROIs was subtracted from the intensity of the first frame after bleaching to normalize the background value to 0. Finally, the results were divided by the initial intensity before photobleaching to normalize the initial value to 1.

To calculate the apparent diffusion coefficient (D_{app}) of p53^{4M} ΔTAD inside DPIC by FRAP (*53*), the normalized curves of ROIs were first fitted by $I_{(t)} = A \cdot (1 - e^{-\tau t})$. $I_{(t)}$ is the normalized protein intensity of each time point, A is the mobile fraction of protein and τ is the recovery time constant. Then, the half time of fluorescent recovery $T_{1/2}$ is calculated by $T_{1/2} = \frac{-ln0.5}{\tau}$. Finally, the D_{app} is calculated by $D_{app} = \frac{0.22\ \omega^2}{T_{1/2}}$. ω indicates the radius of the actual bleached region, which is 1.2 μm in our work.

Fluorescence Correlation Spectroscopy (FCS)

The FCS measurement was performed by a home-made confocal microscope. The detailed information about this setup can be referred to the previous work (*54, 55*). The power of 640nm-laser after the objective was set as 5 μW. The laser focus was 10 μm above the interface of coverslip and water. Cy5-labeled p53^{4M} ΔTAD and Cy5-labeled 400-bp random DNA were diluted to 20 nM by an FCS buffer (8 mM Tris-HCl (pH 7.5), 120 mM NaCl, and 16 mM DTT) and then loaded into the flow cell. Raw data of photon arriving time of Cy5 detection channel (ET700/75m, Chroma) was recorded for 2 min. Data was analyzed by a home-made MATLAB script.

Box-plot

The function of “boxplot” in MATLAB software (R2015a, 64-bit, February 12, 2015) was used to plot the boxplots in Supplementary Fig. 2 and 4. For each boxplot, the red bar represents median. The bottom edge of the box represents 25th percentiles, and the top is 75th percentiles. Most extreme data points are covered by the whiskers except outliers. The '+' symbol is used to represent the outliers.

Unpaired t test

Statistical significance was evaluated based on Student’s t-tests (Prism 9 for macOS, Version 9.1.0 (216), March 15, 2021, GraphPad Software, Inc.). Test was chosen as unpaired t test. P value style: GP: 0.1234 (ns), 0.0332 (*), 0.0021 (**), 0.0002 (***), < 0.0001 (****).

Dimensionless generic model and numerical simulation

The dynamical model (Eq. 1) can be rescaled to the following general system and expressed in terms of rescaled $k_d = 1$ and $D_v = 1$ (see **Supplementary Methods, texts 1.4 for details**)

$$\begin{cases} \frac{\partial U}{\partial T} = -U + (\beta_1 U + b_1)V - \frac{\rho\beta_2}{\beta+U+V}U + \delta\nabla^2 U \\ \frac{\partial V}{\partial T} = U - (\beta_1 U + b_1)V + \frac{\rho\beta_2}{\beta+U+V}U + \nabla^2 V \end{cases} . \quad (4)$$

The interpretation of the parameters in this nondimensionalized model (Eq. 4), their default values, and their definition in terms of the original experimental measurements in our study are given in Table 1 and Supplementary Table 1. As Eq. 4 might prove abstract and unspecific, we conducted numerical simulations based on the dimensionless system (4) to unify mass-conserving systems.

References

1. A. M. Turing, The Chemical Basis of Morphogenesis. *Philos T Roy Soc B* **237**, 37-72 (1952).

2. E. Meron, *Nonlinear physics of ecosystems*. (CRC Press, 2015).

3. J. Swift, P. C. Hohenberg, Hydrodynamic Fluctuations at Convective Instability. *Phys Rev A* **15**, 319-328 (1977).

4. M. C. Cross, P. C. Hohenberg, Pattern-Formation Outside of Equilibrium. *Rev Mod Phys* **65**, 851-1112 (1993).

5. H. Meinhardt, *The algorithmic beauty of sea shells*. (Springer-Verlag, 2009).

6. M. Rietkerk, J. Van de Koppel, Regular pattern formation in real ecosystems. *Trends Ecol Evol* **23**, 169-175 (2008).

7. A. Deblais, A. C. Maggs, D. Bonn, S. Woutersen, Phase Separation by Entanglement of Active Polymerlike Worms. *Phys Rev Lett* **124**, (2020).

8. A. Y. Li *et al.*, Ice needles weave patterns of stones in freezing landscapes. *P Natl Acad Sci USA* **118**, (2021).

9. Q. X. Liu *et al.*, Phase separation explains a new class of self-organized spatial patterns in ecological systems. *P Natl Acad Sci USA* **110**, 11905-11910 (2013).

10. K. Siteur *et al.*, Phase-separation physics underlies new theory for the resilience of patchy ecosystems. *P Natl Acad Sci USA* **120**, (2023).

11. C. P. Brangwynne, P. Tompa, R. V. Pappu, Polymer physics of intracellular phase transitions. *Nat Phys* **11**, 899-904 (2015).

12. J. W. Cahn, Phase Separation by Spinodal Decomposition in Isotropic Systems. *J Chem Phys* **42**, 93-99 (1965).

13. J. W. Cahn, J. E. Hilliard, Free Energy of a Nonuniform System .1. Interfacial Free Energy. *J Chem Phys* **28**, 258-267 (1958).

14. S. Mao, D. Kuldinow, M. P. Haataja, A. Kosmrlj, Phase behavior and morphology of multicomponent liquid mixtures. *Soft Matter* **15**, 1297-1311 (2019).

15. A. Radja, E. M. Horsley, M. O. Lavrentovich, A. M. Sweeney, Pollen Cell Wall Patterns Form from Modulated Phases. *Cell* **176**, 856-868 (2019).

16. J. Wang *et al.*, A Molecular Grammar Governing the Driving Forces for Phase Separation of Prion-like RNA Binding Proteins. *Cell* **174**, 688-699 (2018).

17. T. S. Harmon, A. S. Holehouse, M. K. Rosen, R. V. Pappu, Intrinsically disordered linkers determine the interplay between phase separation and gelation in multivalent proteins. *Elife* **6**, (2017).

18. J. M. Choi, A. S. Holehouse, R. V. Pappu, Physical Principles Underlying the Complex Biology of Intracellular Phase Transitions. *Annu Rev Biophys* **49**, 107-133 (2020).

19. E. Tjhung, C. Nardini, M. E. Cates, Cluster phases and bubbly phase separation in active fluids: Reversal of the Ostwald process. *Physical Review X* **8**, (2018).

20. A. Klosin *et al.*, Phase separation provides a mechanism to reduce noise in cells. *Science* **367**, 464-468 (2020).

21. S. F. Banani, H. O. Lee, A. A. Hyman, M. K. Rosen, Biomolecular condensates: organizers of cellular biochemistry. *Nat Rev Mol Cell Bio* **18**, 285-298 (2017).

22. M. Feric, T. Misteli, Function moves biomolecular condensates in phase space. *Bioessays* **44**, (2022).

23. S. Alberti, A. A. Hyman, Biomolecular condensates at the nexus of cellular stress, protein aggregation disease and ageing. *Nat Rev Mol Cell Biol* **22**, 196-213 (2021).

24. C. Li *et al.*, Deciphering the molecular mechanism of DNA-protein interactive co-condensates. *bioRxiv*, 2024.2001.2026.577305 (2024).

25. L. Wurthner *et al.*, Bridging scales in a multiscale pattern-forming system. *P Natl Acad Sci USA* **119**, (2022).

26. Q. Ouyang, H. L. Swinney, Transition from a Uniform State to Hexagonal and Striped Turing Patterns. *Nature* **352**, 610-612 (1991).

27. F. Brauns, J. Halatek, E. Frey, Phase-Space Geometry of Mass-Conserving Reaction-Diffusion Dynamics. *Phys Rev X* **10**, (2020).

28. M. Otsuji *et al.*, A mass conserved reaction-diffusion system captures properties of cell polarity. *Plos Computational Biology* **3**, 1040-1054 (2007).

29. P. Hinow *et al.*, The DNA binding activity of p53 displays reaction-diffusion kinetics. *Biophys J* **91**, 330-342 (2006).

30. H. Furukawa, A Dynamic Scaling Assumption for Phase-Separation. *Adv Phys* **34**, 703-750 (1985).

31. B. D. Gaulin, S. Spooner, Y. Morii, Kinetics of phase separation in Mn0.67Cu0.33. *Phys Rev Lett* **59**, 668-671 (1987).

32. Y. P. Chen, J. E. Ferrell, colony formation as a condensation phenomenon. *Nature Communications* **12**, (2021).

33. J. D. Murray, *Mathematical biology II: spatial models and biomedical applications*. (Springer, ed. 3rd Edition, 2003).

34. G. Theraulaz *et al.*, Spatial patterns in ant colonies. *P Natl Acad Sci USA* **99**, 9645-9649 (2002).

35. A. Shinozaki, Y. Oono, Asymptotic form factor for spinodal decomposition in three-space. *Physical Review Letters* **66**, 173-176 (1991).

36. P. W. Anderson, More is different. *Science* **177**, 393-396 (1972).

37. J. M. Carlson, G. H. Swindle, Self-organized criticality: sandpiles, singularities, and scaling. *Proceedings of the National Academy of Sciences* **92**, 6712-6719 (1995).

38. P. Bak, C. Tang, K. Wiesenfeld, Self-organized criticality: An explanation of the 1/f noise. *Phys Rev Lett* **59**, 381-384 (1987).

39. P. Bak, C. Tang, K. Wiesenfeld, Self-organized criticality. *Phys Rev A Gen Phys* **38**, 364-374 (1988).

40. B. D. Malamud, J. D. A. Millington, G. L. W. Perry, Characterizing wildfire regimes in the United States. *P Natl Acad Sci USA* **102**, 4694-4699 (2005).

41. B. D. Malamud, G. Morein, D. L. Turcotte, Forest fires: An example of self-organized critical behavior. *Science* **281**, 1840-1842 (1998).

42. F. Brauns, H. Weyer, J. Halatek, J. Yoon, E. Frey, Wavelength Selection by Interrupted Coarsening in Reaction-Diffusion Systems. *Phys Rev Lett* **126**, (2021).

43. J. Halatek, E. Frey, Rethinking pattern formation in reaction-diffusion systems. *Nat Phys* **14**, 507-514 (2018).

44. M. Cross, H. Greenside, *Pattern formation and dynamics in nonequilibrium systems*. (Cambridge University Press, 2009).

45. M. E. Cates, D. Marenduzzo, I. Pagonabarraga, J. Tailleur, Arrested phase separation in reproducing bacteria creates a generic route to pattern formation. *P Natl Acad Sci USA* **107**, 11715-11720 (2010).

46. Z. P. Ge, Q. X. Liu, Foraging behaviours lead to spatiotemporal self-similar dynamics in grazing ecosystems. *Ecol Lett* **25**, 378-390 (2022).

47. Y. Oono, S. Puri, Computationally Efficient Modeling of Ordering of Quenched Phases. *Phys Rev Lett* **58**, 836-839 (1987).

48. J. Berry, S. C. Weber, N. Vaidya, M. Haataja, C. P. Brangwynne, RNA transcription modulates phase transition-driven nuclear body assembly. *P Natl Acad Sci USA* **112**, E5237-E5245 (2015).

49. P. Lu *et al.*, Direct validation of dune instability theory. *Proc Natl Acad Sci USA* **118**, (2021).

50. D. S. W. Lee, N. S. Wingreen, C. P. Brangwynne, Chromatin mechanics dictates subdiffusion and coarsening dynamics of embedded condensates. *Nat Phys* **17**, 531-538 (2021).

51. M. M. C. Tortora, L. D. Brennan, G. Karpen, D. Jost, HP1-driven phase separation recapitulates the thermodynamics and kinetics of heterochromatin condensate formation. *Proceedings of the National Academy of Sciences* **120**, e2211855120 (2023).

52. Y. C. Gao, M. T. Han, S. Shang, H. F. Wang, L. S. Qi, Interrogation of the dynamic properties of-order heterochromatin CRISPR-dCas9. *Mol Cell* **81**, 4287-4299 (2021).

53. J. H. Liu, F. Zhorabek, X. Dai, J. Q. Huang, Y. Chau, Minimalist Design of an Intrinsically Disordered Protein-Mimicking Scaffold for an Artificial Membraneless Organelle. *Acs Central Sci* **8**, 493-500 (2022).

54. S. J. Peng *et al.*, Phase separation at the nanoscale quantified by dcFCCS. *P Natl Acad Sci USA* **117**, 27124-27131 (2020).

55. Y. Yao, W. Wang, C. Chen, Mechanisms of phase-separation-mediated cGAS activation revealed by dcFCCS. *PNAS Nexus* **1**, (2022).

56. G. G. Penny, K. E. Daniels, S. E. Thompson, Local properties of patterned vegetation: quantifying endogenous and exogenous effects. *Philos T R Soc A* **371**, (2013).